

Article

# Large-Scale and Simple Synthesis of NiFe(OH)<sub>x</sub> Electrode Derived from Raney Ni Precursor for Efficient Alkaline Water Electrolyzer

Tianshui Li <sup>1</sup>, Wei Liu <sup>1</sup>, Huijun Xin <sup>1</sup>, Qihao Sha <sup>1</sup>, Haijun Xu <sup>2,\*</sup>, Yun Kuang <sup>1,3,\*</sup>  and Xiaoming Sun <sup>1</sup>

<sup>1</sup> State Key Laboratory of Chemical Resource Engineering, College of Chemistry, University of Chemical Technology, Beijing 100029, China; litianshui@buct.edu.cn (T.L.); liuw@buct.edu.cn (W.L.); xinjh@buct.edu.cn (H.X.); shaqh@buct.edu.cn (Q.S.); sunxm@mail.buct.edu.cn (X.S.)

<sup>2</sup> College of Mathematics and Physics, Beijing University of Chemical Technology, Beijing 100029, China

<sup>3</sup> Ocean Hydrogen Energy R&D Center, Research Institute of Tsinghua University in Shenzhen, Shenzhen 518033, China

\* Correspondence: hjxu@mail.buct.edu.cn (H.X.); kuangy@tsinghua-sz.org (Y.K.)

**Abstract:** Water electrolysis is a crucial technology in the production of hydrogen energy. Due to the escalating industrial demand for green hydrogen, the required electrode size for a traditional alkaline water electrolyzer has been increasing. Numerous studies have focused on developing highly active oxygen evolution reaction (OER) catalysts for water electrolysis. However, there remains a significant gap between the microscale synthesis of catalysts in laboratory settings and the macroscale preparation required for industrial scenarios. This challenge is particularly pronounced in the synthesis of sizable self-supported electrodes. In this work, we employed a commercially available Raney Ni-coated Ni mesh as a precursor material to fabricate a self-supported NiFe(OH)<sub>x</sub>@Raney Ni anode with a substantial dimension exceeding 300 mm through a straightforward immersion technique. The as-prepared electrode exhibited remarkable electrocatalytic OER activity, as an overpotential of only 240 mV is required to achieve 10 mA cm<sup>-2</sup>. This performance is comparable to that of NiFe-LDHs synthesized via a hydrothermal method, which is difficult to scale up for industrial applications. Furthermore, the electrode demonstrated exceptional durability, maintaining stable operation for over 100 h at a current density of 500 mA cm<sup>-2</sup>. The large-scale electrode displayed consistent overpotentials across various areas, indicating uniform catalytic activity. When integrated into an alkaline water electrolysis device, it delivered an average cell voltage of 1.80 V at 200 mA cm<sup>-2</sup> and achieved a direct current hydrogen production energy consumption as low as 4.3 kWh/Nm<sup>3</sup>. These findings underline the suitability of electrodes for industrial scale applications, offering a promising alternative for energy-efficient hydrogen production.

**Keywords:** oxygen evolution reaction; large-scale electrode; alkaline water electrolysis



**Citation:** Li, T.; Liu, W.; Xin, H.; Sha, Q.; Xu, H.; Kuang, Y.; Sun, X. Large-Scale and Simple Synthesis of NiFe(OH)<sub>x</sub> Electrode Derived from Raney Ni Precursor for Efficient Alkaline Water Electrolyzer. *Catalysts* **2024**, *14*, 296. <https://doi.org/10.3390/catal14050296>

Academic Editor: Yat Li

Received: 24 March 2024

Revised: 20 April 2024

Accepted: 26 April 2024

Published: 29 April 2024



**Copyright:** © 2024 by the authors. Licensee MDPI, Basel, Switzerland. This article is an open access article distributed under the terms and conditions of the Creative Commons Attribution (CC BY) license (<https://creativecommons.org/licenses/by/4.0/>).

## 1. Introduction

Hydrogen energy, as a renewable energy source with high energy density, has garnered significant global attention in recent years [1–6]. Based on the analysis of the International Energy Agency (IEA) on the total global final energy consumption, the proportion of hydrogen energy in the total final energy consumption should increase to ~2% by 2030 and ~10% by 2050 [7]. The coupling of renewable energy electricity with water electrolysis devices represents an effective means of producing green hydrogen [8–11]. However, due to the complex four-electron process involved in the oxygen evolution reaction (OER), which exhibits unfavorable reaction kinetics and high overpotentials, numerous researchers have focused on developing highly active OER catalytic electrodes [12–15].

Noble metal based OER catalysts, such as IrO<sub>2</sub> and RuO<sub>2</sub> [16–18], demonstrate high activity but are limited by their exorbitant cost, finite reserves, and stability issues, hindering

their large-scale application. Abundant non-noble metals such as Ni [19–21], Co [22–24], and Fe [25–27] based compounds, including oxides, hydroxides, oxyhydroxides, and layered double hydroxides (LDHs), have shown promise as OER catalysts. As water electrolysis has already achieved industrialization and is witnessing rapidly growing demand, the capacity of individual alkaline water electrolysis devices has reached over 5 GW, with electrode sizes typically exceeding 2 m. Industrial electrodes are commonly produced using plasma spraying methods, where Raney nickel is applied to the cathode substrate surface, while the anode is typically produced via alloy powder spraying due to its feasibility for large-scale, low-cost manufacturing. Consequently, current research on water electrolysis catalytic electrodes should emphasize simplicity in synthesis methods and adaptability to large-scale. Lu et al. [28] reported the application of a  $\text{Cu}_2\text{S@NiS@Ni/NiMo}$  electrocatalyst on a large-scale ( $100\text{ cm}^2$ ) copper foam using a convenient scaling-up method. This electrode exhibited a low hydrogen evolution overpotential of 250 mV at  $1000\text{ mA cm}^{-2}$  and stable operation exceeding 2000 h at  $500\text{ mA cm}^{-2}$ . However, research on large-scale, high-activity water electrolysis anodes remains insufficient.

NiFe-LDHs [29–31] are widely recognized in the scientific community as excellent catalysts for the OER, playing a crucial role in energy conversion and storage systems. However, their performance at high current densities remains a challenge. To address this issue, Sun et al. [32] took an innovative approach by growing NiFe-LDHs directly in situ as nanosheet arrays on Ni foam. This was achieved by placing the Ni foam substrate in an autoclave, allowing for the controlled growth of the nanosheet arrays. Similarly, Duan et al. [33] employed an electrodeposition technique to grow LDH nanosheet arrays on Ni foam. Both methods aim to enhance the OER activity of NiFe-LDHs at high current densities by modifying their nanostructures. The nanosheet arrays, with their unique structure, reduce bubble size during the evolution of gas at the electrode surface. This reduction in bubble size lowers the mass transfer resistance, resulting in lower overpotentials at high current densities. These improved performance characteristics make them more suitable for industrial applications where high current densities and low overpotentials are essential. However, they also present challenges in terms of energy consumption and equipment requirements while these methods show promise in terms of enhancing OER activity. The autoclave and electrodeposition processes can be energy-intensive and require specialized equipment, posing significant obstacles to large-scale, cost-effective production.

In this work, we used commercially available Raney Ni-coated Ni mesh as a precursor to synthesize a large-scale water electrolysis anode  $\text{NiFe(OH)}_x\text{@Raney Ni}$  exceeding  $300\text{ mm}$  by simple immersion in a solution containing  $\text{Ni(NO}_3)_2$  and  $\text{Fe(NO}_3)_3$  at  $60\text{ }^\circ\text{C}$ . The prepared electrode exhibited an overpotential of only 240 mV at a current density of  $10\text{ mA cm}^{-2}$ , comparable to that of hydrothermally synthesized NiFe-LDHs. It also demonstrated stable operation exceeding 100 h at  $500\text{ mA cm}^{-2}$ . The large-scale electrode showed consistent overpotentials across different regions, and when incorporated into an alkaline water electrolysis device, it achieved an average cell voltage of 1.80 V and a direct current hydrogen production energy consumption as low as  $4.3\text{ kWh/Nm}^3$ , demonstrating its viability for industrial applications.

## 2. Results

The synthesis of  $\text{NiFe(OH)}_x\text{@Raney Ni}$  is achieved through a simple two-step immersion method (Figure 1a). Initially, the Raney Ni-coated Ni mesh is thoroughly cleaned and then immersed in a solution containing 30 mM  $\text{Ni(NO}_3)_2$  and 10 mM  $\text{Fe(NO}_3)_3$  at  $60\text{ }^\circ\text{C}$  for 12 h. During this process, due to the presence of Al in Raney Ni and the protons resulting from the hydrolysis of metal nitrate solutions, a slow dissolution of Al occurs, releasing  $\text{H}_2$ . This leads to a local increase in pH, accompanied by the gradual reaction of  $\text{Ni}^{2+}$  and  $\text{Fe}^{3+}$  with  $\text{OH}^-$  to form  $\text{NiFe(OH)}_x$ . However, the amount of Al dissolved in this step is minimal. After the immersion, the electrode is placed in a 2 M KOH solution to dissolve the remaining Al and activate it, following the same procedure as the activation of commercial Raney Ni. The appearance of the electrode changes (Figure 1b) from the original silver

color to a brownish-yellow hue during immersion, indicating the successful synthesis of  $\text{NiFe}(\text{OH})_x$ , as confirmed by the consistent color after Al dissolution and activation in the alkaline solution. In comparison, the Ni mesh without Raney Ni coating exhibits minimal color change after immersion under the same conditions (Figure S1). Scanning Electron Microscopy (SEM) reveals that the original Raney Ni coating consists of uneven spherical particles (Figure 1c). After immersion in the solution containing  $\text{Ni}^{2+}$  and  $\text{Fe}^{3+}$ , nanosheet structures grow on the surface (Figure 1d). Following Al dissolution and activation, the surface becomes more porous while maintaining the nanosheet structures (Figure 1e,f). Energy-Dispersive X-ray Spectroscopy (EDS) elemental mapping of  $\text{NiFe}(\text{OH})_x$ @Raney Ni (Figure 1g) shows uniform distribution of Ni, Fe, and Al elements across the electrode surface. Notably, Al does not completely dissolve in Raney Ni, which aligns with previous applications. Specifically, regarding the remaining Al, we have demonstrated through EDS characterization that the atomic ratio in the material are as follows: Ni is 55.59%, Fe is 23.83%, and Al is 20.59% (Supplementary Material Table S1). Specifically, the atomic ratio of Al in commercially activated Raney Ni is approximately 33%. The remaining Al in the NiAl phase can help maintain this porous structure, providing structural and thermal stability to the catalyst.

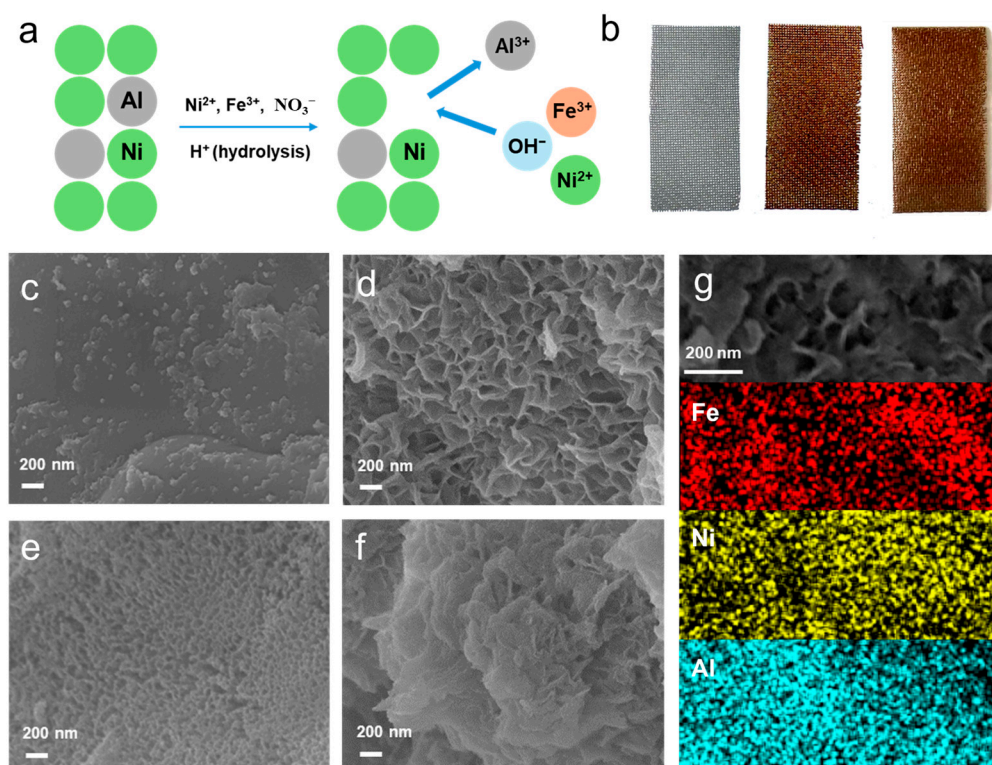


**Figure 1.** (a) Schematic diagram illustrating the synthesis mechanism of  $\text{NiFe}(\text{OH})_x$ @Raney Ni. (b) Left, middle, and right images depict the original Raney Ni, post-immersion, and after etching Al, respectively. SEM images of (c) Raney Ni, (d) Raney Ni after immersion, and (e,f)  $\text{NiFe}(\text{OH})_x$ @Raney Ni obtained after etching Al. (g) SEM image and corresponding EDS elemental mapping of  $\text{NiFe}(\text{OH})_x$ @Raney Ni.

A detailed structural characterization of  $\text{NiFe}(\text{OH})_x$ @Raney Ni was conducted. X-ray diffraction (XRD) patterns were compared for the prepared electrode before and after Al dissolution (Figure 2a). It can be observed that with the dissolution of Al, the characteristic (111) diffraction peak at  $2\theta = 38.47^\circ$ , corresponding to PDF#04-0787 of Al, disappears. On the other hand, peaks located at  $2\theta = 44.5^\circ$ ,  $51.8^\circ$ , and  $76.4^\circ$  correspond to the (111), (200), and (220) crystal planes of Ni (PDF#04-0850), respectively. Notably, the diffraction peak of the Ni (111) crystal plane shifts towards a lower angle with the dissolution of Al.

Two small diffraction peaks can also be observed at  $43.69^\circ$  and  $76.81^\circ$ , corresponding to the (111) and (202) planes of  $\text{AlNi}_3$  (PDF#21-0008), respectively. There was no significant change before and after activation, confirming the existence of  $\text{AlNi}_3$  (Raney Ni), which is consistent with the results obtained through EDS-Mapping. The relatively small diffraction peaks are attributed to the fact that Raney Ni is located beneath the  $\text{NiFe}(\text{OH})_x$  layer. The crystalline phase of elemental Al disappears after activation, but the crystalline phase of  $\text{AlNi}_3$  remains present. This plays a crucial role in maintaining the porous structure of Raney Ni. Additionally, we have identified two characteristic peaks at  $12.40^\circ$  and  $21.45^\circ$ , which correspond to the NiFe compound (PDF#44-1088). X-ray photoelectron spectroscopy (XPS) was employed to analyze the electronic structure of  $\text{NiFe}(\text{OH})_x$ @Raney. The high-resolution spectrum of Ni 2p (Figure 2b) exhibits peaks at 856.03 eV and 873.98 eV, corresponding to Ni 2p<sub>3/2</sub> and 2p<sub>1/2</sub>, respectively, confirming the presence of  $\text{Ni}^{2+}$  in the sample [34]. The peaks at 861.98 eV and 880.13 eV are accompanying satellite peaks. In the high-resolution spectrum of Fe 2p (Figure 2c), peaks located at 711.08 eV and 724.73 eV correspond to 2p<sub>3/2</sub> and 2p<sub>1/2</sub>, respectively, indicating that Fe exists in the form of  $\text{Fe}^{3+}$  on the electrode surface [35]. The peaks at 718.78 eV and 731.68 eV are satellite peaks of 2p<sub>3/2</sub> and 2p<sub>1/2</sub>, respectively. In the high-resolution spectrum of Al 2p (Figure 2d), the peak at 74.08 eV confirms the presence of  $\text{Al}^{3+}$  [36], while the peak at 68.38 eV is attributed to the Ni 3p signal, further supporting the existence of  $\text{Ni}^{2+}$ . In the O 1s high-resolution spectrum (Figure S2), two peaks are present at 531.38 eV and 529.83 eV, corresponding to the OH signal from adsorbed  $\text{H}_2\text{O}$  and the metal-oxygen signal on the electrode surface [37], respectively.

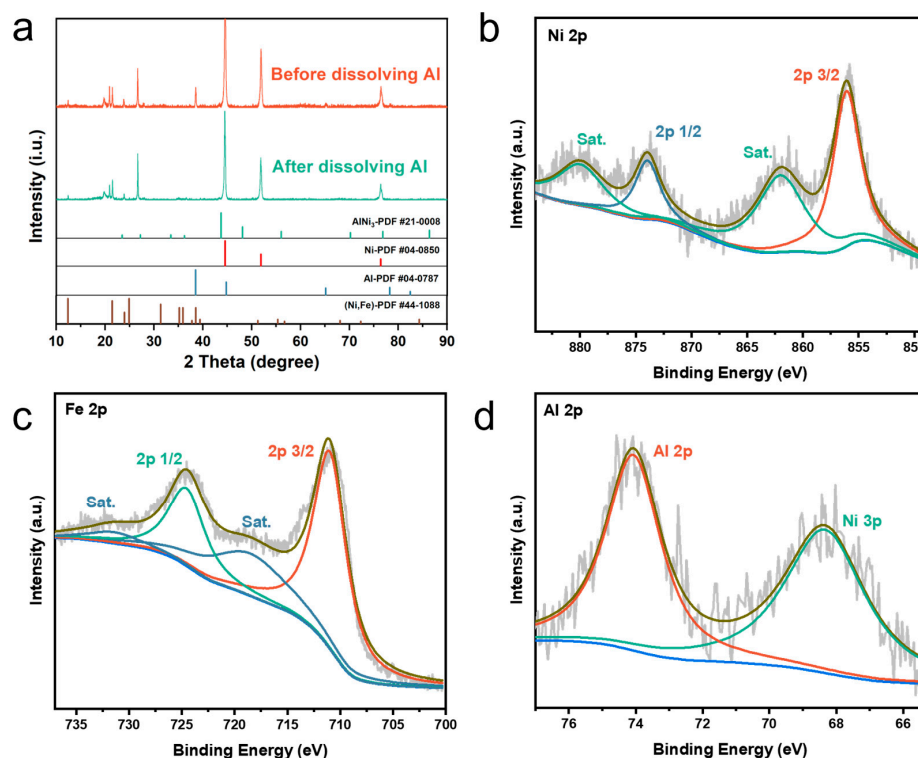


**Figure 2.** (a) XRD patterns of  $\text{NiFe}(\text{OH})_x$ @Raney before and after Al dissolution and activation. High-resolution XPS spectra of  $\text{NiFe}(\text{OH})_x$ @Raney for (b) Ni 2p, (c) Fe 2p, and (d) Al 2p.

The OER activity of  $\text{NiFe}(\text{OH})_x$ @Raney Ni was evaluated using the Cyclic Voltammetry (CV) curves obtained from a three-electrode system (Figure 3a). The as-prepared electrode exhibited an overpotential of only  $240 \text{ mV}@10 \text{ mA cm}^{-2}$  and  $401 \text{ mV}@200 \text{ mA cm}^{-2}$ . For comparison, the  $\text{NiFe-LDHs@Ni}$  mesh synthesized hydrothermally on the Ni mesh surface and the bare Ni mesh showed overpotentials of  $241 \text{ mV}@10 \text{ mA cm}^{-2}$  and  $408 \text{ mV}@200 \text{ mA cm}^{-2}$ , respectively (Figure 3b). We also compared the OER activity of Raney Ni@Ni mesh and bare Ni mesh. The overpotential of Raney Ni@Ni mesh was found to be  $308 \text{ mV}@10 \text{ mA cm}^{-2}$

and  $503 \text{ mV}@200 \text{ mA cm}^{-2}$ , whereas the bare Ni mesh exhibited an overpotential of  $340 \text{ mV}@10 \text{ mA cm}^{-2}$  and  $570 \text{ mV}@200 \text{ mA cm}^{-2}$ . All the performance test curves mentioned above have been IR correction, and the  $R_{\Omega}$  value was determined from the EIS curve (Figure S3). These results demonstrate the superior activity of the  $\text{NiFe}(\text{OH})_x\text{@Raney Ni}$  electrode, which performs comparably to the hydrothermally synthesized  $\text{NiFe-LDHs@Ni}$  mesh and exhibits a more pronounced advantage in overpotential at higher current densities. This enhanced performance may be attributed to the smaller nanosheet size and lower mass transfer resistance of the prepared electrode compared to the hydrothermally synthesized electrode. We further analyzed the reaction kinetics of different electrodes through Tafel curves (Figure 3c). The prepared  $\text{NiFe}(\text{OH})_x\text{@Raney Ni}$  electrode ( $40.7 \text{ mV dec}^{-1}$ ) and  $\text{NiFe-LDHs@Ni}$  mesh ( $40.8 \text{ mV dec}^{-1}$ ) exhibited similar Tafel slopes, both lower than those of  $\text{Raney Ni@Ni}$  mesh ( $58.5 \text{ mV dec}^{-1}$ ) and  $\text{Ni}$  mesh ( $69.5 \text{ mV dec}^{-1}$ ). This confirms that the prepared electrode possesses excellent reaction kinetics, similar to those of the hydrothermally synthesized  $\text{NiFe-LDHs@Ni}$  mesh, which is consistent with their activity test results. Similar to previous reports, the high activity of the prepared catalyst is associated with the synergistic effect between Ni and Fe, and the strong Ni/Fe-O covalency facilitates electron transfer [38]. To verify the stability of the electrode, chronopotentiometry curves were measured in a three-electrode system using  $1 \text{ M KOH}$  electrolyte (Figure 3d). The electrode exhibited stable operation for over  $240 \text{ h}$  at current densities of  $500 \text{ mA cm}^{-2}$ . SEM characterization of the electrode after OER revealed that the nanosheet array structure on the electrode surface was maintained, confirming its high stability. Subsequently, detailed XPS characterization was performed on the electrode after the stability test (Figure S4) to investigate changes in the electronic structure of the electrode surface. Comparison of the high-resolution XPS spectra for Ni before and after OER showed that the main peak of  $2p_{3/2}$  shifted from  $856.03 \text{ eV}$  to  $856.18 \text{ eV}$ , indicating an increase in the Ni valence state. On the contrary, the main peak of  $2p_{3/2}$  in the high-resolution spectrum of Fe shifted from  $711.08 \text{ eV}$  to  $710.78 \text{ eV}$ , suggesting a decrease in the Fe valence state. These observations are consistent with previous comparisons made for  $\text{NiFe-LDHs}$  before and after operation, where an increase in the Ni valence state is favorable for the formation of the OER active species  $\text{NiOOH}$  [39]. On the other hand, the absence of any shift in the peak of  $\text{Al } 2p$  confirmed the stability of valence state of Al and indicated that there was no significant further dissolution.

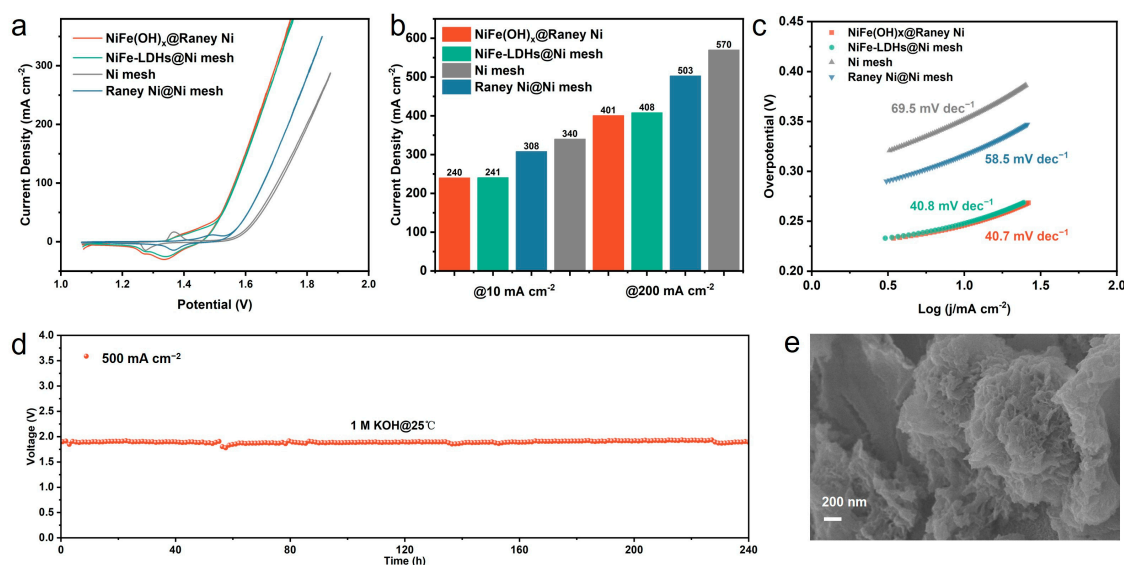


**Figure 3.** (a) CV curves of  $\text{NiFe}(\text{OH})_x\text{@Raney Ni}$ ,  $\text{NiFe-LDHs@Ni}$  mesh  $\text{Raney Ni@Ni}$  mesh and  $\text{Ni}$  mesh. (b) Comparison of overpotentials for  $\text{NiFe}(\text{OH})_x\text{@Raney Ni}$  and the reference electrode. (c) Tafel curves of different electrodes. (d) Chronopotentiometry curves of  $\text{NiFe}(\text{OH})_x\text{@Raney Ni}$  at current density of  $200 \text{ mA cm}^{-2}$  and  $500 \text{ mA cm}^{-2}$ , (e) SEM image of the sample after testing.

Due to the simplicity and low cost of the preparation method, we successfully synthesized a large-scale  $\text{NiFe}(\text{OH})_x\text{@Raney Ni}$  electrode exceeding 300 mm using a larger container and the same experimental approach (Figure 4a). The electrode exhibited a relatively uniform surface color. To further verify the uniformity of the large-scale electrode's performance, we selected five areas on its surface and conducted LSV curve tests for OER performance using a three-electrode system (Figure 4b). The curves showed a high degree of overlap. Further analysis revealed that the overpotentials at a current density of  $10 \text{ mA cm}^{-2}$  for the five regions were 249 mV, 247 mV, 245 mV, 248 mV, and 247 mV, respectively (Figure 4c), demonstrating the successful synthesis of a highly uniform large-scale electrode. Subsequently, an electrolyzer containing two cells was assembled using the prepared electrode as the anode and a commercial Raney Ni electrode as the cathode (Figure 4d). In particular, the anode we used in the electrolyzer was a circular electrode with a diameter of 115 mm, which was obtained by laser-cutting the aforementioned large-area electrode (Figure S5). Each cell of the electrolyzer comprised a cathode, an anode, a bipolar plate, sealing gaskets, and a membrane (Zirfon UTP500, AGFA, Mortsel, Belgium). The assembled electrolyzer was integrated with a gas–liquid separator, temperature controller, and electrolyte circulation pump to form an alkaline water electrolysis device for evaluating the electrode's performance. Constant current tests were conducted on the device at  $80 \text{ }^\circ\text{C}$  and a current density of  $200 \text{ mA cm}^{-2}$  using a 30% KOH electrolyte. The results showed that the electrode could operate stably for over 100 h. During the tests, the average cell voltage of the electrolyzer was 1.8 V, corresponding to a hydrogen production energy consumption of  $4.3 \text{ kWh/Nm}^3$ , which is among the best-performing commercial alkaline electrolyzers. In addition, we used the drainage method to test the Faraday efficiency of  $\text{H}_2$  and  $\text{O}_2$  under different current densities in 50 s. In electrolyzer testing, the theoretical gas production is relatively large (197.25 mL of  $\text{H}_2$  produced under electrolysis at  $150 \text{ mA cm}^{-2}$  for 50 s), which allows for a more accurate evaluation of Faraday efficiency. The data results are shown in Table S2, where the Faraday efficiencies of  $\text{H}_2$  and  $\text{O}_2$  are 99.3% and 99.4, respectively. Overall, the simple synthesis method and high activity of the  $\text{NiFe}(\text{OH})_x\text{@Raney Ni}$  electrode make it a promising candidate for industrial applications.

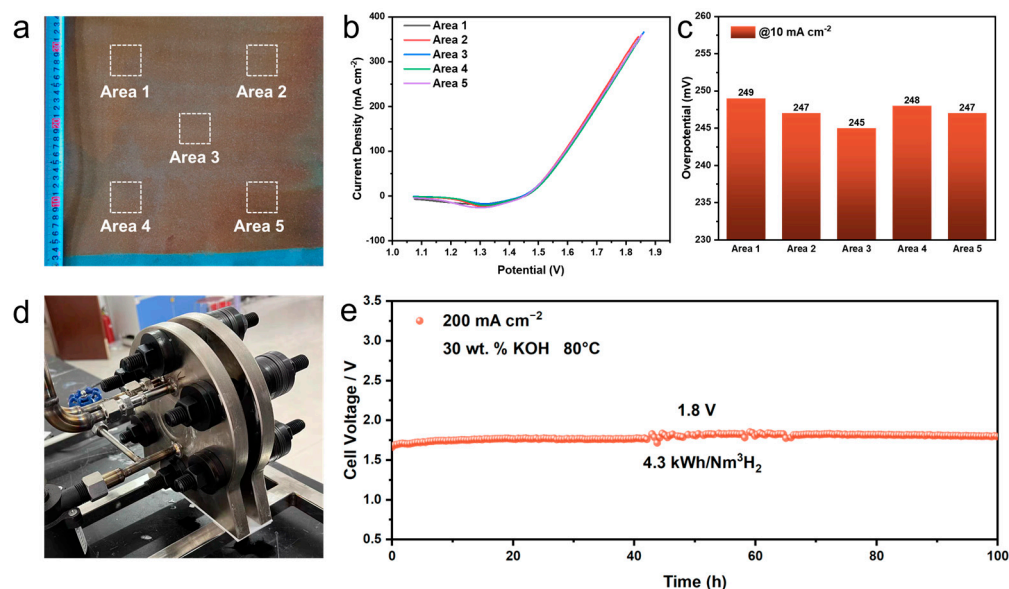


**Figure 4.** (a) Photograph of a large-scale electrode with a side length exceeding 300 mm. (b) LSV curves demonstrating OER activity across different regions of the large-scale electrode. (c) Comparison of OER overpotentials in distinct areas of the large-scale electrode. (d) Image depicting an alkaline water electrolyzer. (e) Evaluation of an alkaline water electrolyzer assembled with the prepared electrode as the anode and a commercial Raney Ni electrode as the cathode. Testing was conducted at a current density of  $200 \text{ mA cm}^{-2}$ , a temperature of  $80 \text{ }^\circ\text{C}$ , and using 30 wt.% KOH electrolyte.

### 3. Material and Methods

#### 3.1. Chemicals

All reagents employed in this study were of analytical grade and utilized as-is, without any need for further purification processes.  $\text{Ni}(\text{NO}_3)_2 \cdot 6\text{H}_2\text{O}$ ,  $\text{Fe}(\text{NO}_3)_3 \cdot 9\text{H}_2\text{O}$ , KOH,  $\text{CO}(\text{NH}_2)_2$ , and  $\text{C}_2\text{H}_5\text{OH}$  were purchased from Shanghai Aladdin Biochemical Technology Co., Ltd., Shanghai, China. Ni mesh and Raney Ni-coated Ni mesh were purchased from Zhangjiakou Ruiqing Technology Co., Ltd., Zhangjiakou, Hebei Province, China. Deionized water was purchased from Hangzhou Wahaha Co., Ltd., Hangzhou, Zhejiang Province, China.

#### 3.2. Synthesis of $\text{NiFe}(\text{OH})_x @ \text{Raney Ni}$

In the initial phase of the experiment, small pieces measuring  $1 \text{ cm} \times 2 \text{ cm}$  were excised from a monolithic Raney Ni-coated Ni mesh. This step was essential to ensure uniformity and controllability in the dimensions of the electrode material for subsequent experimental procedures. Following excision, these pieces were submerged in ethanol and subjected to ultrasonic cleaning, an effective method for eliminating surface impurities and contaminants, thereby ensuring the purity and homogeneity of the electrodes. The material underwent ultrasonic cleaning in ethanol for a duration of 15 min. After the cleaning process, the Raney Ni-coated Ni mesh pieces were removed from the ethanol and placed in a drying oven maintained at  $60^\circ \text{C}$  to eliminate any residual ethanol on the surface and prepare them for the subsequent impregnation step. Next, a solution containing 30 mM  $\text{Ni}(\text{NO}_3)_2 \cdot 6\text{H}_2\text{O}$  and 10 mM  $\text{Fe}(\text{NO}_3)_3 \cdot 9\text{H}_2\text{O}$  was prepared using deionized water, and 50 mL of this solution was dispensed into a beaker. This solution played a pivotal role in the subsequent impregnation process, providing the necessary nickel and iron ions for the synthesis of  $\text{NiFe}(\text{OH})_x$ . Subsequently, the pre-dried  $1 \text{ cm} \times 2 \text{ cm}$  Raney Ni-coated Ni mesh pieces were immersed in the aforementioned solution, ensuring complete submersion. Following impregnation, the beaker containing the solution and the mesh pieces was placed in a  $60^\circ \text{C}$  oven for 12 h. This step aimed to facilitate the reaction between the material surface and the ions in the solution, leading to the formation of  $\text{NiFe}(\text{OH})_x$ . Finally, the electrodes were removed from the solution and rinsed with deionized water to eliminate any excess ions or unreacted substances adhering to the surface. After rinsing, the electrodes were once again placed in the oven for drying. The resulting dried electrodes constituted the desired  $\text{NiFe}(\text{OH})_x @ \text{Raney Ni}$  electrodes. Throughout the entire preparation process, parameters such as temperature, time, and solution concentration were rigorously controlled to ensure the production of electrodes with optimal performance and reproducibility.

#### 3.3. Synthesis of $\text{NiFeLDHs} @ \text{Ni Mesh}$

Initially, the Ni mesh was precisely cut into small rectangular pieces measuring  $1 \text{ cm} \times 2 \text{ cm}$ , suitable for use as electrodes in subsequent experiments. To ensure the removal of any residual organic contaminants, such as oils or greases, from the surface of these electrode pieces, they were immersed in ethanol and subjected to ultrasonic cleaning for a duration of 15 min. This cleaning process effectively dislodged and removed the unwanted surface impurities. Following the ethanol treatment, the electrode pieces were carefully removed and placed in a drying oven to evaporate any residual solvent, ensuring a dry and clean surface for further processing. Next, to eliminate any oxide layer that might have formed on the surface of the Ni mesh during storage or handling, the pieces were transferred to a bath of concentrated hydrochloric acid. Here, they underwent a second ultrasonic cleaning step, lasting for 5 min. This acidic treatment was crucial in removing any oxides that could potentially interfere with subsequent reactions or affect the electrode's performance. After the acid treatment, the electrode pieces were thoroughly rinsed with deionized water to remove any traces of acid or dissolved oxides. In preparation for the synthesis of the desired material, a solution containing the necessary precursors was prepared. Specifically, 35 mL of deionized water was measured into a clean beaker, and to this, precise amounts of  $\text{Ni}(\text{NO}_3)_2 \cdot 6\text{H}_2\text{O}$  (0.5 mmol),  $\text{Fe}(\text{NO}_3)_3 \cdot 9\text{H}_2\text{O}$  (0.5 mmol), and

$\text{CO}(\text{NH}_2)_2$  (5 mmol) were added. These components were mixed and stirred vigorously to ensure complete dissolution and a homogeneous solution. Subsequently, the prepared solution, along with the pre-cleaned Ni mesh electrode pieces, was carefully transferred into a Teflon-lined autoclave. The Teflon lining provided a chemically inert environment, crucial for high-pressure and high-temperature reactions. The autoclave was then sealed and placed in an oven preheated to 120 °C. The reaction was allowed to proceed for 12 h under these controlled conditions, ensuring optimal growth and crystallization of the desired material on the electrode surface. After the reaction time elapsed, the autoclave was removed from the oven and allowed to cool to ambient temperature. The electrode pieces were then carefully retrieved from the reaction mixture and subjected to a final cleaning step. This involved ultrasonic cleaning in deionized water for 5 min to remove any loosely attached particles or impurities that did not grow in situ on the electrode surface during the synthesis process. The resulting product, NiFeLDHs@Ni mesh, exhibited the desired characteristics and was ready for further characterization or use in downstream applications. The entire process, from cutting and cleaning to synthesis and final cleaning, was carefully controlled to ensure reproducibility and consistency in the quality of the electrodes produced.

#### 3.4. Electrochemical Measurements

The electrochemical measurements were executed under ambient conditions within a standardized three-electrode setup enclosed in a glass cell, which was interfaced with a sophisticated electrochemical workstation (specifically, the model CHI 660e from CH Instruments, Shanghai, China). The dimensions of the electrocatalysts were precisely maintained at 1 cm × 1 cm, and these catalysts were directly utilized as the working electrode without any further modifications or treatments. A carbon rod electrode, known for its stability and conductivity, served as the counter electrode in this configuration. Meanwhile, a saturated calomel electrode (SCE) is used to provide a reliable reference potential, ensuring the accuracy of potential measurements throughout the entire experimental process, with a standard electrode potential of  $E_{\text{SCE}} = 0.244 \text{ V}$  (vs. RHE). For the electrolyte, a freshly prepared 1 M KOH solution was utilized, offering a suitable alkaline environment for the electrochemical reactions under investigation. Additionally, the activation process of the catalyst was rigorously assessed through cyclic voltammetry (CV). This technique was performed at a scan rate of  $100 \text{ mV s}^{-1}$  for 20 consecutive cycles, spanning a potential range of 0 to 1 V versus the SCE in the aforementioned electrolyte. This comprehensive approach allowed for a thorough evaluation of the catalyst's electrochemical behavior and activation characteristics. It is important to note that all measured potentials were referenced to the SCE and were subsequently converted to the reversible hydrogen electrode (RHE) scale using the Nernst equation ( $E_{\text{RHE}} = E_{\text{SCE}} + \text{pH} \times 0.059$ ). This conversion ensures compatibility and comparability with other electrochemical studies, facilitating a broader understanding of the system's performance. Polarization curves, which provide valuable insights into the electrode's performance under varying potential conditions, were obtained using Linear sweep voltammetry (LSV) with a scan rate of  $5 \text{ mV s}^{-1}$ . These curves were carefully corrected for Ohmic drops, which were meticulously tested through impedance spectroscopy techniques. This correction is crucial as it accounts for the potential losses due to electrolyte resistance, ensuring accurate and reliable polarization data. Furthermore, electrochemical impedance spectroscopy (EIS) measurements were conducted in the 1 M KOH solution. These measurements involved applying an AC voltage with an amplitude of 5 mV at the open circuit potential, while sweeping the frequency from 100 kHz to 0.1 Hz. EIS provides valuable information on the electrode's electrochemical behavior, particularly its charge transfer characteristics and interfacial reactions, further enhancing our understanding of the system's performance and kinetics.

### 3.5. Materials Characterization

The specimens' dimensions and microscopic structure were meticulously examined using a state-of-the-art field-emission scanning electron microscope (FE-SEM, model JEOL JSM6335, TEM, Tokyo, Japan). Operating at an accelerating voltage of 20 kV, this high-resolution instrument allowed for detailed visualization of the specimens' surface features and microstructures. The FE-SEM analysis was crucial in revealing the specimens' size, shape, and surface morphology, essential for understanding their material properties and potential applications. To further investigate the structural characteristics of the specimens, X-ray diffraction (XRD) measurements were performed. Utilizing a Rigaku D/max 2500 X-ray diffractometer (Tokyo, Japan) equipped with Cu K $\alpha$  radiation, operating under conditions of 40 kV, 30 mA, and a wavelength ( $\lambda$ ) of 1.5418 Å, the XRD patterns were obtained. These patterns provided valuable insights into the specimens' crystalline structure, including phase identification, crystal orientation, and lattice parameters. The measurements were conducted over a  $2\theta$  angular range of 5° to 80°, with a scanning rate of 5° per minute, ensuring a comprehensive analysis of the specimens' structural properties. In addition, to further understand the chemical composition of the sample, X-ray photoelectron spectroscopy (XPS) analysis was also performed, with a source gun type of Al K $\alpha$ , excitation voltage of 15 kV, and lamp current of 10 mA. These analyses were carried out using a PHI Quantera II XPS Scanning Microprobe system (ULVAC-PHI, Inc., Chigasaki, Japan), a highly sensitive instrument capable of detecting the elemental composition and chemical states of the specimens' surfaces. The XPS data provided critical information on the specimens' elemental composition, oxidation states, and bonding configurations, essential for elucidating their chemical properties and potential reactivity. Collectively, these advanced analytical techniques—FE-SEM, XRD, and XPS—offered a comprehensive characterization of the specimens, revealing their size, shape, crystalline structure, and chemical composition. This detailed understanding of the specimens' properties is crucial for further exploring their potential applications and optimizing their performance in various fields.

### 3.6. Performance Evaluation of Alkaline Water Electrolysis Devices

The alkaline water electrolysis devices testing system, sourced from Zhangjiakou Ruiqing Technology Co., Ltd., Zhangjiakou, China, is a comprehensive setup designed to evaluate the performance of alkaline water electrolysis under controlled conditions. This system integrates several key components, including an electrolyzer, gas-liquid separator, DC power supply, electrolyte circulation pump, and a precise temperature control system. The electrolyzer, a core element of the testing system, is configured with two cells, arranged in a manner that allows for efficient and controlled electrochemical reactions. A notable feature of this electrolyzer is the utilization of a composite membrane, specifically the AGFA ZIRFON UTP500, Mortsel, Belgium. Within the electrolytic cell configuration, the anode employs an electrode that was specifically synthesized in the course of this study. This customized electrode is designed to optimize the electrochemical reactions occurring at the anode, thereby enhancing the overall efficiency of the water electrolysis process. Conversely, the cathode is comprised of Raney Ni coated Ni mesh. The testing conditions were carefully controlled to simulate real operational scenarios. Specifically, the temperature was maintained at 80 °C, a temperature commonly employed in alkaline water electrolysis systems due to its favorable impact on electrolyte conductivity and reaction kinetics. Additionally, the electrolyte circulation rate was set at 6 L/min to ensure adequate mixing and heat transfer within the electrolyzer. In terms of data acquisition and analysis, the cell voltage is calculated as half of the total voltage measured across both cells. This calculation accounts for the fact that the electrolyzer operates with two cells in series. Furthermore, the DC energy consumption is determined by multiplying the cell voltage by a factor of 2.39, a coefficient that takes into account various system-specific parameters such as electrolyte resistivity and cell geometry.

#### 4. Conclusions

In this work, the NiFe(OH)<sub>x</sub>@Raney Ni self-supported anode was scaled synthesized through a simple one-step immersion method. The as-prepared electrode exhibits excellent OER performance, requiring only 240 mV of overpotential to achieve 10 mA cm<sup>-2</sup>. Moreover, the electrode demonstrates stable operation for over 100 h at an industrial required current density of 500 mA cm<sup>-2</sup>. This straightforward approach enables the large-scale synthesis of the electrode (with a side length exceeding 300 mm). When incorporated as the anode in an alkaline water electrolyzer, the average cell voltage is only 1.80 V at 200 mA cm<sup>-2</sup>, resulting in a low hydrogen production energy consumption of 4.3 kWh/Nm<sup>3</sup>. This study provides a novel avenue for the future preparation of large-scale, high-activity OER catalytic electrodes.

**Supplementary Materials:** The following supporting information can be downloaded at: <https://www.mdpi.com/article/10.3390/catal14050296/s1>, Figure S1: Images of bare Ni mesh before and after immersing in a solution containing Ni<sup>2+</sup> and Fe<sup>3+</sup> at 60 °C for 12 h; Figure S2: The high-resolution XPS spectrum of O 1s for NiFe(OH)<sub>x</sub>@Raney Ni; Figure S3: EIS test curves for different electrodes; Figure S4: A comparison of the high-resolution XPS spectra for (a) Ni 2p, (b) Fe 2p, and (c) Al 2p before and after the OER stability test; Figure S5: Appearance of the anode surface assembled into the electrolyzer; Table S1: The ratio of various elements characterized by EDS; Table S2: Faraday efficiency testing of H<sub>2</sub> and O<sub>2</sub> in the electrolyzer.

**Author Contributions:** Conceptualization, T.L. and X.S.; methodology, T.L. and H.X. (Huijun Xin); validation, T.L.; investigation, T.L. and H.X. (Huijun Xin), writing—original draft preparation, T.L. and Q.S.; writing—review and editing, W.L., H.X. (Haijun Xu) and Y.K.; visualization, T.L.; supervision, W.L., H.X. (Haijun Xu) and Y.K.; funding acquisition, Y.K. and X.S. All authors have read and agreed to the published version of the manuscript.

**Funding:** This work was supported by the Science and Technology Innovation Foundation of Laoshan Laboratory (No. LSKJ202205700), the Xinjiang Uygur Autonomous Region Key R&D Projects (No. 202114958) and Shenzhen Energy Co., Ltd. The authors also thanks for National Key R&D Program of China (2021YFA1502200), the National Natural Science Foundation of China, the Key Research Project of Beijing Natural Science Foundation.

**Data Availability Statement:** The data presented in this study are available on request from the corresponding author.

**Conflicts of Interest:** The authors declare that this study received funding from Shenzhen Energy Co., Ltd. The funder was not involved in the study design, collection, analysis, interpretation of data, the writing of this article or the decision to submit it for publication.

#### References

1. Yu, Z.Y.; Duan, Y.; Feng, X.Y.; Yu, X.X.; Gao, M.R.; Yu, S.H. Clean and Affordable Hydrogen Fuel from Alkaline Water Splitting: Past, Recent Progress, and Future Prospects. *Adv. Mater.* **2021**, *33*, 35. [CrossRef]
2. Wang, S.; Lu, A.L.; Zhong, C.J. Hydrogen production from water electrolysis: Role of catalysts. *Nano Converg.* **2021**, *8*, 23. [CrossRef]
3. Cullen, D.A.; Neyerlin, K.C.; Ahluwalia, R.K.; Mukundan, R.; More, K.L.; Borup, R.L.; Weber, A.Z.; Myers, D.J.; Kusoglu, A. New roads and challenges for fuel cells in heavy-duty transportation. *Nat. Energy* **2021**, *6*, 462–474. [CrossRef]
4. Kovac, A.; Paranos, M.; Marcus, D. Hydrogen in energy transition: A review. *Int. J. Hydrogen Energy* **2021**, *46*, 10016–10035. [CrossRef]
5. Zhou, K.L.; Wang, Z.L.; Han, C.B.; Ke, X.X.; Wang, C.H.; Jin, Y.H.; Zhang, Q.Q.; Liu, J.B.; Wang, H.; Yan, H. Platinum single-atom catalyst coupled with transition metal/metal oxide heterostructure for accelerating alkaline hydrogen evolution reaction. *Nat. Commun.* **2021**, *12*, 10. [CrossRef]
6. Tarhan, C.; Çil, M.A. A study on hydrogen, the clean energy of the future: Hydrogen storage methods. *J. Energy Storage* **2021**, *40*, 10. [CrossRef]
7. Morales, T.C.; Oliva, V.R.; Velazquez, L.F. Hydrogen from Renewable Energy in Cuba. In Proceedings of the ISES Solar World Congress (SWC), Cancun, Mexico, 3–7 November 2013; pp. 867–876.
8. Zou, C.N.; Xiong, B.; Xue, H.Q.; Zheng, D.W.; Ge, Z.X.; Wang, Y.; Jiang, L.Y.; Pan, S.Q.; Wu, S.T. The role of new energy in carbon neutral. *Petroleum Explor. Dev.* **2021**, *48*, 480–491. [CrossRef]

9. Zhu, Z.X.; Jiang, T.L.; Ali, M.; Meng, Y.H.; Jin, Y.; Cui, Y.; Chen, W. Rechargeable Batteries for Grid Scale Energy Storage. *Chem. Rev.* **2022**, *122*, 16610–16751. [[CrossRef](#)]
10. Kakoulaki, G.; Kougiyas, I.; Taylor, N.; Dolci, F.; Moya, J.; Jäger-Waldau, A. Green hydrogen in Europe—A regional assessment: Substituting existing production with electrolysis powered by renewables. *Energy Conv. Manag.* **2021**, *228*, 19. [[CrossRef](#)]
11. Ueckerdt, F.; Bauer, C.; Dirnaichner, A.; Overall, J.; Sacchi, R.; Luderer, G. Potential and risks of hydrogen-based e-fuels in climate change mitigation. *Nat. Clim. Chang.* **2021**, *11*, 384. [[CrossRef](#)]
12. Zhang, L.J.; Jang, H.; Liu, H.H.; Kim, M.G.; Yang, D.J.; Liu, S.G.; Liu, X.E.; Cho, J. Sodium-Decorated Amorphous/Crystalline RuO<sub>2</sub> with Rich Oxygen Vacancies: A Robust pH-Universal Oxygen Evolution Electrocatalyst. *Angew. Chem. Int. Ed.* **2021**, *60*, 18821–18829. [[CrossRef](#)]
13. Liang, Q.H.; Brocks, G.; Bieberle-Hutter, A. Oxygen evolution reaction (OER) mechanism under alkaline and acidic conditions. *J. Phys. Energy* **2021**, *3*, 7. [[CrossRef](#)]
14. Jiang, J.; Zhou, X.L.; Lv, H.G.; Yu, H.Q.; Yu, Y. Bimetallic-Based Electrocatalysts for Oxygen Evolution Reaction. *Adv. Funct. Mater.* **2023**, *33*, 29. [[CrossRef](#)]
15. Zhou, D.J.; Li, P.S.; Lin, X.; McKinley, A.; Kuang, Y.; Liu, W.; Lin, W.F.; Sun, X.M.; Duan, X. Layered double hydroxide-based electrocatalysts for the oxygen evolution reaction: Identification and tailoring of active sites, and superaerophobic nanoarray electrode assembly. *Chem. Soc. Rev.* **2021**, *50*, 8790–8817. [[CrossRef](#)]
16. Liu, H.; Zhang, Z.; Fang, J.J.; Li, M.X.; Sendeku, M.G.; Wang, X.; Wu, H.Y.; Li, Y.P.; Ge, J.J.; Zhuang, Z.B.; et al. Eliminating over-oxidation of ruthenium oxides by niobium for highly stable electrocatalytic oxygen evolution in acidic media. *Joule* **2023**, *7*, 558–573. [[CrossRef](#)]
17. Liu, H.; Zhang, Z.; Li, M.X.; Wang, Z.L.; Zhang, X.H.; Li, T.S.; Li, Y.P.; Tian, S.B.; Kuang, Y.; Sun, X.M. Iridium Doped Pyrochlore Ruthenates for Efficient and Durable Electrocatalytic Oxygen Evolution in Acidic Media. *Small* **2022**, *18*, 8. [[CrossRef](#)]
18. Liu, H.; Wang, Z.L.; Li, M.X.; Zhao, X.P.; Duan, X.X.; Wang, S.Y.; Tan, G.Y.; Kuang, Y.; Sun, X.M. Rare-earth-regulated Ru-O interaction within the pyrochlore ruthenate for electrocatalytic oxygen evolution in acidic media. *Sci. China Mater.* **2021**, *64*, 1653–1661. [[CrossRef](#)]
19. Xie, J.Y.; Wang, F.L.; Zhou, Y.A.; Dong, Y.W.; Chai, Y.M.; Dong, B. Internal Polarization Field Induced Hydroxyl Spillover Effect for Industrial Water Splitting Electrolyzers. *Nano-Micro Lett.* **2024**, *16*, 12. [[CrossRef](#)]
20. Guo, X.; Li, J.; Meng, F.; Qin, D.; Wu, X.; Lv, Y.; Guo, J. Ru nanoparticles modified Ni<sub>3</sub>Se<sub>4</sub>/Ni(OH)<sub>2</sub> heterostructure nanosheets: A fast kinetics boosted bifunctional overall water splitting electrocatalyst. *J. Colloid Interface Sci.* **2024**, *663*, 847–855. [[CrossRef](#)] [[PubMed](#)]
21. Patil, R.; Rajput, A.; Matsagar, B.M.; Chen, N.C.R.; Ujihara, M.; Salunkhe, R.R.; Yadav, P.; Wu, K.C.W.; Chakraborty, B.; Dutta, S. Elevated temperature-driven coordinative reconstruction of an unsaturated single-Ni-atom structure with low valency on a polymer-derived matrix for the electrolytic oxygen evolution reaction. *Nanoscale* **2024**, *16*, 7467–7479. [[CrossRef](#)] [[PubMed](#)]
22. Zhu, X.Y.; Lyu, J.; Wang, S.S.; Li, X.C.; Wei, X.Y.; Chen, C.; Kooamornpattana, W.; Verpoort, F.; Wu, J.S.; Kou, Z.K. Hierarchical cobalt-molybdenum layered double hydroxide arrays power efficient oxygen evolution reaction. *Nano Res.* **2024**, 1–7. [[CrossRef](#)]
23. Xiao, Z.H.; Huang, Y.C.; Dong, C.L.; Xie, C.; Liu, Z.J.; Du, S.Q.; Chen, W.; Yan, D.F.; Tao, L.; Shu, Z.W.; et al. *Operando* Identification of the Dynamic Behavior of Oxygen Vacancy-Rich Co<sub>3</sub>O<sub>4</sub> for Oxygen Evolution Reaction. *J. Am. Chem. Soc.* **2020**, *142*, 12087–12095. [[CrossRef](#)]
24. Zhao, S.L.; Tan, C.H.; He, C.T.; An, P.F.; Xie, F.; Jiang, S.; Zhu, Y.F.; Wu, K.H.; Zhang, B.W.; Li, H.J.; et al. Structural transformation of highly active metal-organic framework electrocatalysts during the oxygen evolution reaction. *Nat. Energy* **2020**, *5*, 881–890. [[CrossRef](#)]
25. Anantharaj, S.; Kundu, S.; Noda, S. “The Fe Effect”: A review unveiling the critical roles of Fe in enhancing OER activity of Ni and Co based catalysts. *Nano Energy* **2021**, *80*, 16. [[CrossRef](#)]
26. Liang, C.W.; Zou, P.C.; Nairan, A.; Zhang, Y.Q.; Liu, J.X.; Liu, K.W.; Hu, S.Y.; Kang, F.Y.; Fan, H.J.; Yang, C. Exceptional performance of hierarchical Ni-Fe oxyhydroxide@NiFe alloy nanowire array electrocatalysts for large current density water splitting. *Energy Environ. Sci.* **2020**, *13*, 86–95. [[CrossRef](#)]
27. Yu, L.; Wu, L.B.; McElhenny, B.; Song, S.W.; Luo, D.; Zhang, F.H.; Yu, Y.; Chen, S.; Ren, Z.F. Ultrafast room-temperature synthesis of porous S-doped Ni/Fe (oxy)hydroxide electrodes for oxygen evolution catalysis in seawater splitting. *Energy Environ. Sci.* **2020**, *13*, 3439–3446. [[CrossRef](#)]
28. Xu, W.W.; Ma, T.F.; Chen, H.C.; Pan, D.H.; Wang, Z.F.; Zhang, S.X.; Zhang, P.; Bao, S.J.; Yang, Q.H.; Zhou, L.H.; et al. Scalable Fabrication of Cu<sub>2</sub>S@NiS@Ni/NiMo Hybrid Cathode for High-Performance Seawater Electrolysis. *Adv. Funct. Mater.* **2023**, *33*, 9. [[CrossRef](#)]
29. Jia, Y.; Zhang, L.Z.; Gao, G.P.; Chen, H.; Wang, B.; Zhou, J.Z.; Soo, M.T.; Hong, M.; Yan, X.C.; Qian, G.R.; et al. A Heterostructure Coupling of Exfoliated Ni-Fe Hydroxide Nanosheet and Defective Graphene as a Bifunctional Electrocatalyst for Overall Water Splitting. *Adv. Mater.* **2017**, *29*, 8. [[CrossRef](#)]
30. Zhang, H.J.; Li, X.P.; Hähnel, A.; Naumann, V.; Lin, C.; Azimi, S.; Schweizer, S.L.; Maijenburg, A.W.; Wehrspohn, R.B. Bifunctional Heterostructure Assembly of NiFe LDH Nanosheets on NiCoP Nanowires for Highly Efficient and Stable Overall Water Splitting. *Adv. Funct. Mater.* **2018**, *28*, 10. [[CrossRef](#)]

31. Chen, G.B.; Wang, T.; Zhang, J.; Liu, P.; Sun, H.J.; Zhuang, X.D.; Chen, M.W.; Feng, X.L. Accelerated Hydrogen Evolution Kinetics on NiFe-Layered Double Hydroxide Electrocatalysts by Tailoring Water Dissociation Active Sites. *Adv. Mater.* **2018**, *30*, 7. [[CrossRef](#)]
32. Lu, Z.Y.; Xu, W.W.; Zhu, W.; Yang, Q.; Lei, X.D.; Liu, J.F.; Li, Y.P.; Sun, X.M.; Duan, X. Three-dimensional NiFe layered double hydroxide film for high-efficiency oxygen evolution reaction. *Chem. Commun.* **2014**, *50*, 6479–6482. [[CrossRef](#)]
33. Li, Z.H.; Shao, M.F.; An, H.L.; Wang, Z.X.; Xu, S.M.; Wei, M.; Evans, D.G.; Duan, X. Fast electrosynthesis of Fe-containing layered double hydroxide arrays toward highly efficient electrocatalytic oxidation reactions. *Chem. Sci.* **2015**, *6*, 6624–6631. [[CrossRef](#)]
34. Qiu, Z.; Tai, C.W.; Niklasson, G.A.; Edvinsson, T. Direct observation of active catalyst surface phases and the effect of dynamic self-optimization in NiFe-layered double hydroxides for alkaline water splitting. *Energy Environ. Sci.* **2019**, *12*, 572–581. [[CrossRef](#)]
35. Yin, S.M.; Tu, W.G.; Sheng, Y.; Du, Y.H.; Kraft, M.; Borgna, A.; Xu, R. A Highly Efficient Oxygen Evolution Catalyst Consisting of Interconnected Nickel-Iron-Layered Double Hydroxide and Carbon Nanodomains. *Adv. Mater.* **2018**, *30*, 9. [[CrossRef](#)]
36. Magg, N.; Immaraporn, B.; Giorgi, J.B.; Schroeder, T.; Bäumer, M.; Döbler, J.; Wu, Z.L.; Kondratenko, E.; Cherian, M.; Baerns, M.; et al. Vibrational spectra of alumina- and silica-supported vanadia revisited: An experimental and theoretical model catalyst study. *J. Catal.* **2004**, *226*, 88–100. [[CrossRef](#)]
37. Li, T.; Zhao, X.; Sendeku, M.G.; Zhang, X.; Xu, L.; Wang, Z.; Wang, S.; Duan, X.; Liu, H.; Liu, W.; et al. Phosphate-decorated Ni<sub>3</sub>Fe-LDHs@CoP<sub>x</sub> nanoarray for near-neutral seawater splitting. *Chem. Eng. J.* **2023**, *460*, 141413. [[CrossRef](#)]
38. Zhang, H.; Guan, D.; Gu, Y.; Xu, H.; Wang, C.; Shao, Z.; Guo, Y. Tuning synergy between nickel and iron in Ruddlesden-Popper perovskites through controllable crystal dimensionalities towards enhanced oxygen-evolving activity and stability. *Carbon Energy* **2024**, e465. [[CrossRef](#)]
39. Klaus, S.; Cai, Y.; Louie, M.W.; Trotochaud, L.; Bell, A.T. Effects of Fe Electrolyte Impurities on Ni(OH)<sub>2</sub>/NiOOH Structure and Oxygen Evolution Activity. *J. Phys. Chem. C* **2015**, *119*, 7243–7254. [[CrossRef](#)]

**Disclaimer/Publisher’s Note:** The statements, opinions and data contained in all publications are solely those of the individual author(s) and contributor(s) and not of MDPI and/or the editor(s). MDPI and/or the editor(s) disclaim responsibility for any injury to people or property resulting from any ideas, methods, instructions or products referred to in the content.